
ORIGINAL ARTICLE

Journal Section

Flux gradient relations and their dependence on turbulence anisotropy

Samuele Mosso¹ | Marc Calaf^{2†} | Ivana Stiperski^{1*}

¹Department of Atmospheric and Cryospheric Sciences, University of Innsbruck, Innsbruck 6020, Austria,

²Department of Mechanical Engineering, University of Utah, Salt Lake City, Utah 84112, USA

Correspondence

Mosso S., Department of Atmospheric and Cryospheric Sciences, University of Innsbruck, Innsbruck 6020, Austria
Email: samuele.mosso@uibk.ac.at

Present address

*ivana.stiperski@uibk.ac.at
†marc.calaf@utah.edu

Funding information

These results are part of a project that has received funding from the European Research Council (ERC) under the European Union's Horizon 2020 research and innovation program (Grant agreement No. 101001691)

Monin-Obukhov similarity theory (MOST) is used in virtually every Earth System Model (ESM) to parameterize the near-surface turbulent exchanges and mean variables' profiles. Despite its wide spread use, there is high uncertainty in the literature about the appropriate parameterizations to be used. In addition, MOST has limitations in very stable and unstable regimes, over heterogeneous terrain and complex orography, and has been found to incorrectly represent the surface fluxes. A new approach including turbulence anisotropy as a non-dimensional scaling parameter has recently been developed, and has been shown to overcome these limitations and generalize the flux-variance relations to complex terrain.

In this paper we analyze the flux-gradient relations for five well known datasets, ranging from flat and homogeneous to slightly complex terrain. The scaling relations show substantial scatter and highlight the uncertainty in the choice of parameterization even over canonical conditions. We show that by including information on turbulence anisotropy as an additional scaling parameter, the original scatter becomes well bounded and new formulations can be developed, that drastically improve the accuracy of the flux-gradient relations for wind shear (ϕ_M) in unstable conditions, and for temperature gradient (ϕ_H) both in unstable and stable regime. This analysis shows that both ϕ_M and ϕ_H are strongly dependent on turbulence anisotropy and allows to finally

settle the extensively discussed free convection regime for ϕ_M , which clearly exhibits a $-1/3$ power law when anisotropy is accounted for.

Furthermore we show that the eddy diffusivities for momentum and heat and the turbulent Prandtl number are strongly dependent on anisotropy and that the latter goes to zero in the free convection limit.

These results highlight the necessity to include anisotropy in the study of near surface atmospheric turbulence and lead the way for theoretically more robust simulations of the boundary layer over complex terrain.

KEYWORDS

atmospheric surface layer, boundary layer turbulence, complex terrain, Monin Obukhov, near-surface exchange, similarity scaling

1 | INTRODUCTION

The atmospheric boundary layer (ABL) is the region of the atmosphere contained between the Earth's surface and the mostly inviscid free troposphere. As a result, the ABL is driven by the local surface forcing at the bottom (e.g. friction, heating/cooling, evaporation, etc.), and the larger scale flow dynamics of the free atmosphere at the top. It is within this region that most common weather patterns develop, and thus its understanding and accurate representation in Earth System Models (ESMs) of different resolution scales is critical. The flow in the ABL is generally turbulent, with turbulent motions ranging from scales of millimeters (i.e. Kolmogorov microscale) up to a few kilometers (i.e. the height of the ABL, z_i), making its full computational representation a chimera with current computing power (Calaf et al., 2023). Near the surface, within the so-called atmospheric surface layer (ASL) where the energetic turbulent eddies scale with the distance from the wall, the numerical representation of the physical processes is even more challenging. To bypass these limitations, surface-atmosphere interactions are commonly parameterized using Monin-Obukhov similarity theory (MOST) (Monin and Obukhov, 1954; Foken, 2006). This approach is employed in most ESMs, regardless of whether they are turbulence resolving (e.g. Large-Eddy Simulations, LES), or not (i.e. mesoscale, weather prediction and climate models) and is thus a key component in the correct representation of surface-atmosphere exchange on all scales of motion (Edwards et al., 2020). Here we continue to extend the applicability of MOST from flat and horizontally homogeneous terrain (canonical conditions), for which it was developed, to more general surface conditions characterized by orography and surface heterogeneity (cf., Stiperski and Calaf, 2023).

MOST states that in the absence of subsidence (mean downward vertical flow), under steady-state conditions (weak time dependence of turbulence statistics), and horizontal homogeneity of the mean flow statistics, turbulence in ASL (characterized by semi-constancy of fluxes with height) can be fully described by the ratio of buoyancy production/destruction and shear production, represented by the non-dimensional length scale $\zeta = z/L$, also known as the stability parameter (Stull, 1988). In this relation, z is the height above ground, representative of the characteristic length-scale of near-surface turbulence, and L is the Obukhov length (Obukhov, 1971; Stull, 1988) formed by the surface friction velocity ($u_* = (\overline{u'w'^2} + \overline{v'w'^2})^{1/4}$, where $\overline{u'w'}$ and $\overline{v'w'}$ are the streamwise and spanwise momen-

tum flux), the surface buoyancy flux ($\overline{w'\theta'_s}$), buoyancy parameter ($g/\overline{\theta}_v$), and von Kármán constant ($\kappa \approx 0.4$), such that $L = -u_*^3 \overline{\theta}_v / \kappa g \overline{w'\theta'_s}$. According to MOST, any properly non-dimensionalized mean variable in the ASL is solely a function of ζ (Monin and Obukhov, 1954).

When MOST is applied to the profiles of mean wind and temperature, it leads to the so-called flux-gradient (or flux-profile) scaling relations, defined as

$$\begin{aligned}\phi_M(\zeta) &= \frac{\kappa z}{u_*} \frac{d\overline{u}}{dz}, \\ \phi_H(\zeta) &= \frac{\kappa z}{\theta_{v*}} \frac{d\overline{\theta}}{dz},\end{aligned}\tag{1}$$

where the temperature scale is defined as $\theta_* = -\overline{w'\theta'_s}/u_*$. In neutrally stratified ASL conditions, i.e. in the absence of background stratification when the buoyancy flux $\overline{w'\theta'_s}$ tends to zero, ζ also tends to zero, the flux-gradient relations reduce to the famous law-of-the-wall (Pope, 2000) for momentum $\phi_M \sim 1$, and similarly for temperature gradient to $\phi_H \sim Pr_t$, where Pr_t is the turbulent Prandtl number (Pope, 2000).

In non-neutral conditions the shape of the ϕ_M and ϕ_H functions requires empirical determination, and was thus initially developed through extensive experimental measurements. For example, the pioneering Kansas 1968 experiment performed over the ideally spatially homogeneous wheat fields, is the basis for the development of the so-called Businger-Dyer flux-gradient relations (Businger et al., 1971). These relations were modified (Högström, 1988), and ultimately formalized (Högström, 1996, hereon referred to as HÖ96) to the following form:

$$\begin{aligned}\phi_M &= \begin{cases} (1 - \gamma_M \zeta)^{-1/4} & \zeta < 0 \\ 1 + \beta_M \zeta & \zeta > 0 \end{cases} \quad \text{and} \\ \phi_H &= \begin{cases} Pr_t (1 - \gamma_H \zeta)^{-1/2} & \zeta < 0 \\ 1 + \beta_H \zeta & \zeta > 0 \end{cases},\end{aligned}\tag{2}$$

where the β_M , γ_M , β_H , and γ_H are empirical constants given in Tables 1 and 2.

Subsequent measurement campaigns allowed the community to derive refined scaling relations that take into account the behavior of ϕ_M and ϕ_H in both the very stable and unstable regimes which were understudied in the previous campaigns. In the unstable regime (Table 1 and Figure 1), where $\zeta < 0$, the HÖ96 parametrizations follow $\phi_M \sim (-\zeta)^{-1/4}$ and $\phi_H \sim (-\zeta)^{-1/2}$ power laws. These power laws, however, do not conform to the free convective limit in which u_* is no longer a relevant scaling velocity. Instead, Grachev et al. (2000) and (Li, 2021) used scaling arguments and analytical theory to predict a $\phi_{M,H} \sim -\zeta^{-1/3}$. Finally, Kader and Yaglom (1990) proposed a different model based on directional dimensional analysis that postulates the presence of three sub-layers (dynamic, dynamic-convective and convective) with different dynamics in the range of values of ζ . In particular, their model predicts that $\phi_M \sim \zeta^{1/3}$ in the convective sub-layer when $\zeta < -1$, in opposition to the previous arguments. Two equivalent analytical forms of the model are reported in this study by Kader and Perepelkin (1989) and Brutsaert (1992).

In the very stable regime ($\zeta > 1$), a flattening of ϕ_M and ϕ_H is typically encountered, deviating from the linear Businger-Dyer relations (Cheng and Brutsaert, 2005; Grynanik et al., 2020; Beljaars and Holtslag, 1991, see Table 2 and Fig. 1). However, Grachev et al. (2013), and later Babić et al. (2016), clearly showed that data with a Richardson number lower than the critical value ($Ri \leq Ri_c \approx 0.21, 0.25$) follow the Businger-Dyer relations, and postulated that

TABLE 1 Parametrizations of the flux-gradient relations in unstable regime.

Author and abbreviation	Φ_M	Φ_H
Högström (1996), HÖ96	$(1 - 19\zeta)^{-\frac{1}{4}}$	$0.96 (1 - 11.6\zeta)^{-\frac{1}{2}}$
Grachev et al. (2000), GR00	$(1 - 10\zeta)^{-\frac{1}{3}}$	$(1 - 34\zeta)^{-\frac{1}{3}}$
Kader and Yaglom (1990), KY90	$\left(\frac{1 + 0.6\zeta^2}{1 - 7.5\zeta}\right)^{\frac{1}{3}}$	$0.64 \left(\frac{3 - 2.5\zeta}{1 - 10\zeta + 50\zeta^2}\right)^{\frac{1}{3}}$
Brutsaert (1992), <i>alternative formulation of KY90</i>	$\frac{0.37 - 0.24 \zeta ^{0.72}}{0.37 + \zeta ^{0.72}} - 0.5\zeta^{1/3}$	$\frac{0.33 + 0.057 \zeta ^{0.78}}{0.33 + \zeta ^{0.78}}$

the above mentioned flattening stems from the inclusion of non-Kolmogorov turbulence for which MOST is not valid. In this very stable regime, Boyko and Vercauteren (2023) used a stochastic approach to derive a two-dimensional probability density function for ϕ_M , incorporating stochastic effects of submesoscale motions and intermittency into its description.

The non-uniqueness of scaling relations for ϕ_M and ϕ_H in the very stable and unstable regimes even over flat and homogeneous terrain points to MOST's limited applicability not only under restrictive surface conditions, but also outside of a narrow stability range. Additionally, in very stable stratification MOST is considered to be affected by self-correlation (Klipp and Mahrt, 2004). Alternatively, local similarity scaling (Nieuwstadt, 1984) can be used in cases where the constant flux assumption fails, e.g. stable stratification (e.g., Grachev et al., 2005) or over complex terrain (e.g., de Franceschi et al., 2009; Babić et al., 2016; Sfyri et al., 2018; Stiperski et al., 2019). In this approach, the local Obukhov length Λ that varies with height is used instead of L .

Over complex terrain (such as heterogeneous surfaces or orography) multiple assumptions of MOST are clearly violated, and thus the validity of MOST is far from guaranteed. Still, a number of recent studies have shown that if the upstream fetch is homogeneous, MOST can still be valid even over complex terrain, such as for specific wind sectors in an alpine valley (de Franceschi et al., 2009) and an arctic fjord (Kral et al., 2014). At the same time, Babić et al. (2016) observed deviations from MOST even over a wide valley floor, while Martí et al. (2022) found disagreement with MOST very close to the surface in periods of high soil moisture and high solar irradiance. On a steep alpine slope Nadeau et al. (2013) found local scaling to be inadequate due to the presence of katabatic flows and the corresponding decrease of wind speed and change of sign of the vertical wind shear above the katabatic jet maximum. Several efforts, however, have also pointed to a possibility of extending MOST scaling to complex terrain. For example, Hang et al. (2021) showed that non-dimensional wind shear below the katabatic jet can be successfully scaled if the stability parameter is corrected to include the tangent of the slope angle, while Barskov et al. (2018) derived a semi-empirical length scale that includes the effects of canopy and orography to extend MOST to a forested hill.

TABLE 2 Parametrizations of the flux-gradient relations in stable regime.

Author and abbreviation	Φ_M	Φ_H
Högström (1996), HÖ96	$1 + 5.3\zeta$	$1 + 8\zeta$
Cheng and Brutsaert (2005), CB05	$1 + 6.1 \cdot \left(\frac{\zeta + \zeta^{2.5} (1 + \zeta^{2.5})^{-\frac{1.5}{2.5}}}{\zeta + (1 + \zeta^{2.5})^{\frac{1}{2.5}}} \right)$	$1 + 5.3 \cdot \left(\frac{\zeta + \zeta^{1.1} (1 + \zeta^{1.1})^{-\frac{0.1}{1.1}}}{\zeta + (1 + \zeta^{1.1})^{\frac{1}{1.1}}} \right)$
Beljaars and Holtslag (1991), BH91	$1 + \zeta + \frac{2}{3}\zeta \cdot (6 - 0.35\zeta) \cdot e^{-0.35\zeta}$	$1 + \zeta \cdot \left[1 + \frac{2}{3}\zeta \right]^{\frac{1}{2}} + \frac{2}{3}\zeta \cdot (6 - 0.35\zeta) \cdot e^{-0.35\zeta}$
Gryanik et al. (2020), GR20	$1 + \frac{5\zeta}{(1 + 0.3\zeta)^{\frac{2}{3}}}$	$0.98 \left(1 + \frac{5\zeta}{1 + 0.4\zeta} \right)$

Recently, Stiperski and Calaf (2018), Stiperski et al. (2019), Stiperski et al. (2021a) and Stiperski et al. (2021b) showed that turbulence anisotropy encodes the complexity of the boundary conditions forcing the turbulent flow, and thus can be leveraged as a missing parameter in MOST to account for the flow conditions violating MOST assumptions. Stiperski and Calaf (2018) and Stiperski et al. (2019) showed that anisotropy explains 80% of the scatter in the scaling relations of velocity and temperature variances, as well as the scaled turbulence kinetic energy (TKE) dissipation rates observed both over flat and highly complex terrain. Based on these results, Stiperski and Calaf (2023) developed a first generalized extension of MOST, including turbulence anisotropy as an additional non-dimensional parameter into the flux-variance relations, that proved successful over a wide range of terrain types (from flat to mountain top) and stratifications ($|\zeta| \gg 1$) - conditions where basic assumptions of MOST are clearly violated and MOST is known to fail. Indeed, the importance of accounting for the anisotropy of turbulence eddies was already highlighted by Katul et al. (2011) and Salesky et al. (2013) among others when developing the analytical model for ϕ_M from a modified O'KEYPS equation (Li et al., 2012). The promising new approach of including anisotropy into scaling (Stiperski and Calaf, 2023) shows the potential to cover the gap between the idealized, flat and homogeneous and narrow stability range results of the Kansas experiment and complex terrain scaling, however, its applicability to the flux-gradient relations, used in all ESMs to parametrize the surface-atmosphere exchange, has not been explored thus far. While it is arguable that the embedded simplified assumptions of MOST remain justified over the traditional coarse resolution, characteristic in numerical models until recent years, with the continuous increase in computing power and the progressive refinement of grid resolutions this approach is not necessarily valid any longer (Stoll et al., 2020). This is especially the case in configurations with heterogeneous surface conditions, where intrinsic spatial averaging is now challenged (Bou-Zeid et al., 2020). Therefore, developing a generalized MOST scaling with extended applicability to ASL flows in both idealized and perturbed surface conditions is critical for the ABL research and modeling communities. The purpose of this paper is therefore to extend the MOST flux-gradient scaling relations to a wide range of terrain conditions and the entire measurable stability range by including the information on turbulence anisotropy.

The paper is organized as follows: Section 2 introduces the measure of turbulence anisotropy, the datasets used and the methods employed to analyze them. Sections 3 and 4 present the state of the art scaling relations and their extension using turbulence anisotropy. In Section 5 the implications of the novel scaling relations, the limits of their validity and future applications into modelling are discussed, while conclusions are presented in Section 6.

2 | DATA AND METHODS

2.1 | Turbulence Anisotropy in the Atmospheric Boundary Layer

Isotropy is a mathematical symmetry defined as the invariance to rotation and reflection. In the definition by Kolmogorov (1941), a turbulent flow is locally isotropic if the statistical properties (i.e. probability distributions) of the flow's velocity fluctuations and their products at a given point are independent of the spatial and temporal coordinates (homogeneous) and independent from any rotation and reflection of the coordinate system. Isotropy constitutes one of the pillars of turbulence theory and is often taken to be valid at small scales (inertial and dissipation ranges) where turbulence is assumed to have forgotten its generation by anisotropic boundary conditions (Kolmogorov, 1941). At the larger, energy containing scales, turbulence is anisotropic due to the anisotropic nature of the external forcing acting preferentially in specific directions. For example, in shear driven turbulence energy is predominantly injected into the streamwise component, while in buoyancy driven turbulence it is in the vertical component. Alternatively, wall blocking, as well as stable stratification cause preferential energy reduction in the vertical direction (Wyngaard, 2010).

While many studies of ABL turbulence employ the aspect ratio of velocity variances as a proxy for turbulence anisotropy (e.g. Zilitinkevich et al., 2013), here we quantify it through the analysis of the Reynolds stress tensor's invariants (cf., Pope, 2000). The anisotropy invariants are derived from the normalized anisotropic contribution of the Reynolds stress tensor, the Reynolds anisotropy tensor

$$b_{ij} = \frac{\overline{u'_i u'_j}}{\overline{u'_i u'_i}} - \frac{1}{3} \delta_{ij}. \quad (3)$$

An infinite number of sets of two invariants can be derived from a purely anisotropic, therefore traceless, symmetric tensor (cf., Lumley and Newman, 1977). Following Stiperski and Calaf (2023), here we use the barycentric set of invariants (x_b, y_b) as introduced by Banerjee et al. (2007), defined as

$$\begin{aligned} x_b &= \lambda_1 - \lambda_2 + \frac{1}{2}(3\lambda_3 + 1) \\ y_b &= \frac{\sqrt{3}}{2}(3\lambda_3 + 1). \end{aligned} \quad (4)$$

where λ_i are the eigenvalues of the anisotropy tensor b_{ij} (Pope, 2000), which satisfy that

$$\sum_{i=1}^3 \lambda_i = 0 \quad \text{and} \quad \lambda_1 > \lambda_2 > \lambda_3. \quad (5)$$

This barycentric mapping of the eigenvalues organizes all realizable states of turbulence into a triangular, equilateral region and gives equal weight to all of the limiting states of anisotropy and is thus preferred over the principal set of invariants as originally introduced by Lumley and Newman (1977).

Studying the eigenvalues of b_{ij} , the rank of $\overline{u'_i u'_j}$ and its symmetries, allows identifying three asymptotic states that correspond to the three vertices of the barycentric map (Pope, 2000). For three component (isotropic) turbulence, $\overline{u'_i u'_j}$ has rank three (three non-zero eigenvalues), its eigenvalues are equal, while b_{ij} is the null tensor and has all zero eigenvalues. This limiting case is represented by the top corner $(0.5, \sqrt{3}/2)$ of the barycentric map. For two component (axisymmetric) turbulence, $\overline{u'_i u'_j}$ has rank two (two non-zero eigenvalues) and is invariant through rotations and reflections around an axis, in which case the two non-zero eigenvalues of $\overline{u'_i u'_j}$ are equal and the eigenvalues of b_{ij} are $\lambda_1 = \lambda_2 = 1/6$ and $\lambda_3 = -1/3$. This state corresponds to $(x_b, y_b) = (0, 0)$, bottom-left corner. For one component turbulence $\overline{u'_i u'_j}$ has rank one (one non-zero eigenvalue), while the eigenvalues of b_{ij} are $\lambda_1 = 2/3$ and $\lambda_{2,3} = -1/3$. This state is represented in the bottom-right corner of the baricentric map: $(1, 0)$.

The x_b coordinate thus spans from the two component axisymmetric ($x_b = 0$) to the one component ($x_b = 1$) limit, representing information on the componentiality of $\overline{u'_i u'_j}$, while the y_b coordinate ranges from anisotropic ($y_b = 0$) to isotropic turbulence ($y_b = \sqrt{3}/2$).

Following earlier work of Stiperski et al. (2019) and Stiperski and Calaf (2023), the second coordinate of the barycentric map (y_b) will be used as a representative measure of turbulence anisotropy (referred hereon as the *degree of anisotropy*), and will be introduced as an additional non-dimensional variable in the traditional Monin-Obukhov scaling framework of the atmospheric surface layer to generalize the scaling of the surface gradients.

TABLE 3 Information on the datasets used.

Dataset name	Experiment	Location	Terrain	Slope angle	Surface	3D sonic anemometer heights [m]	Thermocouple heights [m]	Time extension
AHATS	AHATS	Kettleman City, California	Flat and homogeneous	< 0.5	Short grass stubble	1.55, 3.3, 4.24, 5.53, 7.08, 8.05	1.51, 3.26, 4.23, 5.47, 7.01, 8.01	2 months, Jun-Aug 2008
CASES99	CASES-99	Kansas	Flat and homogeneous	< 0.5	Grassland	5, 10, 20, 30, 40, 50, 55	5, 10, 20, 30, 40, 50, 55	3 weeks, Oct 1999
METCRAX	METCRAX II NEAR	Meteor Crater, Arizona	Gentle slope	1	Desert	3, 10, 15, 20, 25, 30, 35, 40, 45, 50	3, 10, 15, 20, 25, 30, 35, 40, 45, 50	1 month, Oct 2013
TREX	T-Rex Central	Owens Valley, California	Flat valley floor	< 0.5	Desert	5, 10, 15, 20, 25, 30	5,15,30	2 months, Mar-May 2006
TREXW	T-Rex West	Owens Valley, California	Gentle slope	3.25	Desert	5, 10, 15, 20, 25, 30	5,15,30	2 months, Mar-May 2006

2.2 | Datasets and postprocessing

To study the flux-gradient relations over a wide range of terrain conditions, data from four field campaigns, including five multilevel meteorological towers equipped with high frequency sonic anemometers and low frequency thermocouples, was analyzed. Table 3 contains relevant information on the datasets used.

The Cooperative Atmosphere – Surface Exchange Study 1999 (CASES-99; Poulos et al., 2002), the Advection Horizontal Array Turbulence Study (AHATS; Salesky et al., 2013) and the NEAR tower from the Second Meteor Crater Experiment (METCRAX II; Lehner et al., 2016), represent conditions close to the ideal horizontally homogeneous and flat terrain. The NEAR tower, however, had a non zero slope angle allowing deep katabatic flows to form (Stiperski et al., 2020). In addition, the Central and West towers from the Terrain-induced Rotor Experiment (T-Rex; Grubišić et al., 2008) represent more complex terrain. T-Rex took place in the Owen Valley, a long straight valley with a well-defined sharp ridge on the west side. The Central tower was located at the valley floor while the West tower was placed on the western alluvial slope.

The raw 20 Hz data were double rotated at each height into the streamline coordinate system (x is the streamwise, y the spanwise, and z the surface-normal coordinate) and block averaged to 1 min for stable and 30 min for unstable stratification, with prior linear detrending. The averaging period was determined based on the multiresolution flux decomposition (Howell and Mahrt, 1997), as motivated and used by Stiperski and Calaf (2018); Stiperski et al. (2019); Stiperski and Calaf (2023) and recommended by Casasanta et al. (2021). The mean potential temperature ($\bar{\theta}$) was determined from the slow response thermocouple measurements with a measurement resolution of 1 min. The stability regime was determined from the sign of the buoyancy flux $\overline{w'\theta'_v}$, and only the profiles for which all levels exhibited the same sign of the buoyancy flux were considered in the analysis.

To evaluate the vertical gradients required in the flux-gradient relations, the profiles of mean wind speed $\frac{d\bar{u}}{dz}$ and temperature $\frac{d\bar{\theta}}{dz}$ were interpolated and their derivative at each level was analytically computed. The mean wind speed profiles were interpolated using analytical fitting, with the function $U(z) = a + b \cdot z + c \cdot \log(z)$ constraining

$a = -c \cdot \log(z_0)$. Here z_0 is the roughness length. In the presence of a low level jet a higher-order fitting function was used $U(z) = a + b \cdot z + c \cdot z^2 + d \cdot \log(z)$, constraining $a = -d \cdot \log(z_0)$. The use of the roughness length as a fixed fitting parameter has proven to be the best approach, reducing the scatter of the flux-gradient relations in near-neutral regime. While the fitting functions used here are very simple, they do not produce the high number of artifacts for some complex shaped low level jet cases, which would occur if higher order terms were included. To interpolate the temperature profiles, the general additive model (Hastie, 2017) using fourth degree polynomial smoothing splines was applied (python class `scipy.interpolate.UnivariateSpline`). This method was chosen for its flexibility and because it leads to lower fitting error. For the T-Rex campaign datasets (TREX and TREXW), where only three levels of thermocouples were available, a simple log-linear interpolation $\theta(z) = a + b \cdot z + c \cdot \log(z)$ was used, filtering out cases of low level jet since they produce complex shaped temperature profiles. Smoothing splines were not used to fit the wind profiles because the method produces a suspiciously high neutral limit and more scatter, due to the tendency of the splines to overestimate the local curvature of the profiles and the gradient in the first measurement level.

Roughness length z_0 for each site was estimated from logarithmic fit, $U(z) = \frac{u_*}{\kappa} \log(\frac{z}{z_0})$ to the 5-minute averaged neutral ($|\zeta| < 0.02$) profiles and the measured u_* .

Data were quality controlled for stationarity and well resolved heat flux. Thus stably stratified data for which $|\overline{w'\theta'}| < 0.001K \cdot ms^{-1}$ were filtered out (cf., Klipp and Mahrt, 2004; Nadeau et al., 2013). Stationarity was assured based on the standard test by Foken and Wichura (1996) at its accepted threshold of 30%. In stable regime, the stationarity was required for the mean wind speed, buoyancy flux and momentum flux. Afterwards, consecutive one-minute-averaged profiles of fluxes and mean variables were re-averaged to 10 minutes intervals to reduce the random error. In the unstable regime, stationarity of the mean wind speed and buoyancy flux were required with a 30% threshold; stationarity of the momentum flux was left unconstrained due to low values of the momentum flux in the convective regime.

The flux and gradient Richardson numbers

$$Ri_f = \frac{g}{\theta} \frac{\overline{w'\theta'}}{\overline{u'w'} \frac{d\bar{u}}{dz}}, \quad (6)$$

$$Ri = \frac{g}{\theta} \frac{\frac{d\bar{\theta}}{dz}}{\frac{d\bar{u}}{dz}^2},$$

were required to be below 0.25 (cf., Grachev et al., 2013; Babić et al., 2016). In case of a low level jet, only the wind speed gradient from measurements below the jet maximum height were considered. Additionally, cases of counter-gradient fluxes where $\overline{u'w'} \frac{d\bar{u}}{dz} > 0$ or $\overline{\theta'w'} \frac{d\bar{\theta}}{dz} > 0$, were filtered out.

In the stable regime, applying stationarity criteria reduces the number of 1-min periods to 40% (averaging through the five datasets), with TREXW tower being the most affected dataset (20% surviving). After re-averaging the stationary data to 10 minutes blocks, the Richardson number criteria leaves 70% of data points available and the number of non-countergradient cases averages to 50% for temperature and 60% for wind profiles surviving the previous criteria. On average one third of the stationary re-averaged data points is present in the quality controlled data. In the unstable regime, where the averaging period is 30 minutes, the impact of the quality criteria is much lower, with 90% of stationary points and 80-90% of down-gradient cases.

TABLE 4 Number of data points and relative percentage population of the ensemble dataset in the two stability regimes.

regime	data points	AHATS	CASES99	METCRAX	TREX	TREXW
Stable	36765	28.4	9.0	18.8	28.9	14.9
Unstable	24008	25.6	7.2	18.6	23.3	25.2

2.3 | Formulating new scaling relations

To create new parametrizations including y_b in the flux-gradient relations, we used local scaling, as is common in other scaling studies (cf., Stiperski and Calaf, 2023). The high quality data from each dataset was first merged into an ensemble further used for the analysis. The total number of data points and the relative percentages of points in each individual datasets are shown in Table 4. Fitting the model directly to this ensemble allows the analysis to cover a variety of terrain types and meteorological conditions, with the best model being a reasonable estimate of the average dependence of the scaling relations on stability and anisotropy. This method, however, leads to an uneven representation of each dataset in the ensemble, due to the different amount of data points per site, and does not allow assessing inter-dataset differences. Thus, the robustness of this method will be addressed below.

The new parametrizations were obtained in the following way. For each target variable (ϕ_M, ϕ_H) and separately for the unstable and stable regime, a basis curve was chosen among the ones available in literature (cf., Tables 1 and 2) based on its ability to reproduce the evident features of the data in an optimal way. The bi-variate robust fit was then used to fit the chosen curve to the ensemble data, and determine the coefficients (α_i) of the model. Since the dependence of the model coefficients on anisotropy has to be prescribed, we first determined whether the model should have a linear or a non-linear dependence on y_b by dividing the data into bins of y_b and fitting the curve to each bin, and then examining the resulting $\alpha_i(y_b)$ curves, as in Stiperski and Calaf (2023). Once the best functional form of $\phi(\zeta, y_b)$ was chosen for each case, the coefficients of the obtained model were tuned by minimization of the Huber loss function (Huber, 1992, using the python function `scipy.optimize.least_squares` with `loss = 'huber'`), a more robust alternative to the ordinary least squares method.

The performance of the model was compared to that of the HÖ96 parametrizations, using the skill score defined as:

$$SS = 1 - \frac{MAD_{new}}{MAD_{HÖ96}} \quad (7)$$

where the MAD is the median of the absolute value of the logarithmic residuals $\{|\log(\phi_{data}) - \log(\phi_{model}(\zeta, y_b))|\}$, $MAD_{HÖ96}$ is the MAD using the HÖ96 parametrizations and MAD_{new} is the MAD of the new model including the dependence on y_b .

To assess if the differences in representation between datasets could influence the result, each model (separately for stable and unstable, windspeed and temperature) was tested for compatibility against the average model between the five datasets. To do so, the ensemble data was bootstrapped a thousand times with replacement into groups of half the number of points of the original ensemble dataset and the model $\phi(\zeta, y_b)$ refit to each sample; for every parameter $\alpha_{i,ens}$ of the model, the standard deviation $\sigma_{i,ens}$ was calculated. Then, the same model was trained on each

of the five datasets separately and the average $\alpha_{i,avg}$ between the five estimates was calculated for each parameter. If the difference in the weight of each dataset does not influence the results, the average model between the five datasets and the ensemble data model would be the same. To test this hypothesis, Student's t-test was used on every parameter, comparing the ensemble data estimate and the average-of-five-datasets estimate, using a 5% significance level: $t_i = \frac{|\alpha_{i,ens} - \alpha_{i,avg}|}{\sigma_{i,ens}} < 1.96$. Results of this procedure are discussed in Section 5.

Finally, to assess inter-dataset differences, a-posteriori leave-one-out crossvalidation was applied to each model. This procedure consists in training the model on a subsample of data containing all datasets minus one and validated on the one left out of training calculating the skill score. This allows to assess differences between the datasets and reduce the bias in the assessment of the overall performance that is caused by validating a model on the same data on which it is trained.

For visualization purposes, when plotting the scaling relations, data are binned into logarithmically distributed bins of ζ , defined through the local Obukhov length. This choice does not affect the analysis but gives a better visualization of the data, since ζ is exponentially distributed.

3 | FLUX-GRADIENT SCALING RELATIONS AND THE ROLE OF TURBULENCE ANISOTROPY

We next explore the validity of the universal scaling relations for the windspeed and temperature profiles. As illustrated in Figure 1, the literature ϕ_M curves (Table 1) in the unstable regime for $\zeta > -0.5$ show good agreement amongst themselves and are supported by the data. For $\zeta < -0.5$, however, the data scatter increases and it is unclear which power law the data are following. The presence of substantial scatter in this regime indicates the existence of a missing explanatory variable as argued by Salesky and Chamecki (2012). The disagreement also partially stems from the fact that the classical studies leading to the accepted scaling relations only considered data up to $\zeta \approx -2$, while the range of data used in this study extends down to $\zeta = -100$. Under stable stratification, the wind speed gradient ϕ_M is well represented by a linear function of ζ , as in the scaling relations of Högström (1996). Grachev et al. (2013) and Babić et al. (2016) showed that this is a consequence of filtering out data with a supercritical Richardson numbers, which would otherwise show a leveling off at high stabilities.

The scaled potential temperature gradient ϕ_H in the unstable regime is overall higher than predicted by classical scaling curves (Table 1). Due to large scatter it is also unclear which power law the data are following. On the other hand, the stable regime ϕ_H could also be well represented by a linear model, as argued for ϕ_M , however, it is clear that the HÖ96 curve is not representative of the available data. Furthermore a great amount of scatter is present around $\zeta = 0.1$.

In order to further investigate the observed scatter and to understand the behavior of the dimensionless gradients, we next bin the data according to the degree of turbulence anisotropy, y_b (Figure 2). Once the data are clustered based on the degree of turbulence anisotropy, different scaling behaviors emerge, suggestive of the relevance of turbulence anisotropy as an additional independent parameter, missing in traditional MOST scaling. In the unstable regime this parameter's variability accounts for a significant portion of the observed scatter. In fact, the data show that for anisotropic turbulence the normalized velocity gradient follows the scaling behavior of Kader and Yaglom (1990) closely, with a $-\zeta^{1/3}$ power law, while for more isotropic turbulence, the scaling curves follow the same power law but with progressively lower multiplication coefficients. The debate between the existence of a $1/3$ versus $-1/3$ power law in the free convective limit, where $\zeta < -1$, has been ongoing since the 1980s (Högström, 1988). While the $-1/3$ power law can be inferred from analytical arguments (namely the O'KEYPS equation, Li, 2021), no analytical

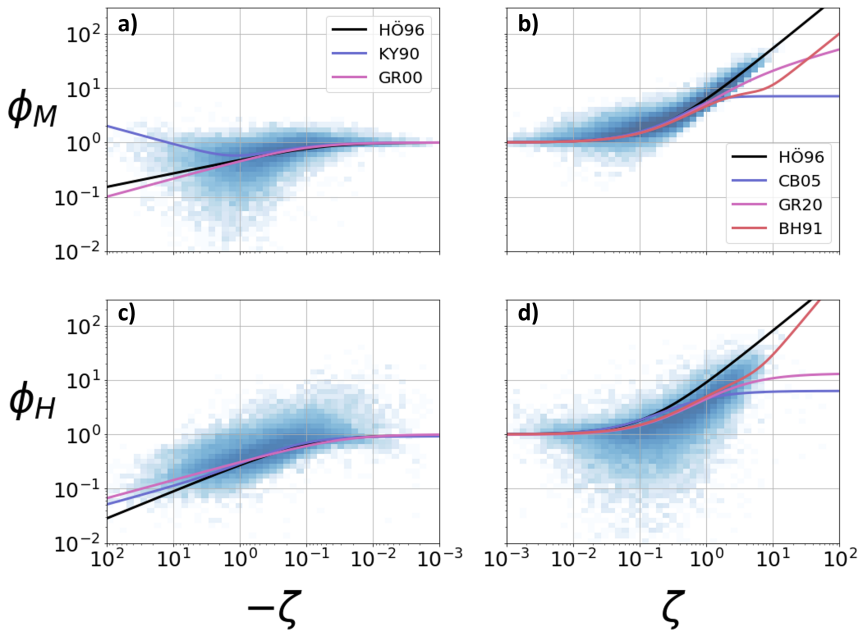


FIGURE 1 Two-dimensional histogram of flux-gradient relations for the ensemble dataset for the mean wind speed (a,b) and temperature (c,d) profile under unstable (a,c) and stable (b,d) stratification. Literature curves from Tables 2 and 1 are shown in color.

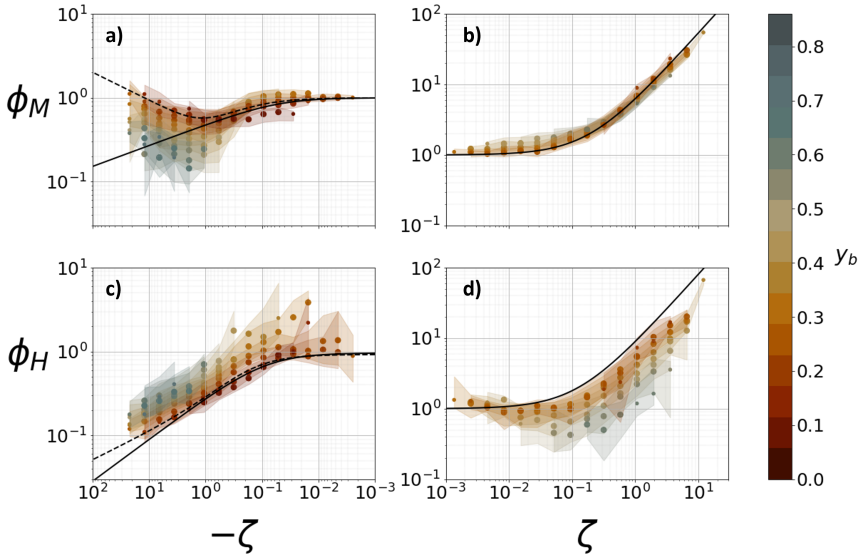


FIGURE 2 As in Figure 1 but for data binned according to the degree of anisotropy y_b (color bar). The black lines represent the HÖ96 parametrizations, while the dashed lines in the unstable regime represent the KY90.

model has been able to predict the $+1/3$ behaviour, which can nevertheless be derived by directional dimensional analysis (Kader and Yaglom, 1990) and scaling arguments. In fact, in the free convective limit where u_* is no longer a relevant parameter, having $\phi_M \sim -\zeta^{1/3}$ will cancel out the dependence on friction velocity on both sides of the equation. The same result is achieved by considering the free convection velocity $w_{fc} = \left[\frac{g}{\theta} \overline{w' \theta' z} \right]^{1/3}$ as the relevant velocity scale. As argued by Li (2021), however, this asymptotic behaviour $\phi_M \sim -\zeta^{1/3}$ is in contradiction with the O'KEYPS equation, which is based on the assumption of a constant asymptotic limit of the Prandtl turbulent number, Pr_t . Interestingly, results in Figure 2 illustrate that in the highly convective range, ϕ_M effectively increases, and thus the turbulent Prandtl will go to zero as showed in Section 5.4, highlighting the ineffectiveness of the O'KEYPS model when $\zeta < -1$. In contrast, ϕ_M in the stable regime shows little dependence on anisotropy.

In parallel, turbulence anisotropy explains substantial scatter of ϕ_H under both stratifications. In the unstable regime similarly to ϕ_M , ϕ_H shows a clear dependence on y_b , with anisotropic data following the scaling behaviour of Kader and Yaglom (1990), while isotropic data are parallel but with higher values. In the the stable regime, anisotropy accounts for the majority of the scatter in ϕ_H , but the scaled data highlight the need to correct the slope of the HÖ96 parametrization.

4 | GENERALIZED PARAMETRIZATION OF THE FLUX-GRADIENT SCALING RELATIONS

4.1 | Unstable regime

As shown in Sect. 3, the ϕ_M in the unstable regime binned according to anisotropy y_b (Figure 1a) clearly support the model of Kader and Yaglom (1990), which we use to develop the new scaling relations including anisotropy. The KY90 model exists in two functional forms as introduced in Kader and Perepelkin (1989) and Brutsaert (1992). We

follow the Brutsaert (1992) formulation due to its simpler form that allows easier interpolation to the ensemble data (cf. Table 1):

$$\phi_M = \frac{a(y_b) + b|\zeta|^{n(y_b)}}{a(y_b) + |\zeta|^{n(y_b)}} - c(y_b) \cdot \zeta^{\frac{1}{3}}. \quad (8)$$

Here a , n and c are the model coefficients (α_i) and are linear functions of y_b . The procedure for determining the best model and tuning it is described in Section 2.

Fitting the model results in the following relations:

$$a = \begin{cases} 0.24 - 0.38y_b & y_b < 0.6 \\ 0.012 & y_b > 0.6, \end{cases}$$

$$b = 0.061,$$

$$c = 0.45 - 0.53y_b,$$

$$n = -0.12 + 6.4y_b,$$

where the parameter a is constrained to be positive. The resulting curves for each anisotropy bin are shown in Figure 3a.

Similar results are obtained for ϕ_H in the unstable regime. When ϕ_H is binned according to anisotropy (Figure 1c) it clearly shows that the KY90 formulation should be employed. Of the two functional forms following the Kader and Yaglom (1990) model, the one from Kader and Perepelkin (1989) is chosen here, since the function provided by Brutsaert (1992) has a constant asymptotic limit that does not agree with the power law predicted in the convective sub-layer ($\zeta^{-1/3}$), as supported by the data. The chosen model then takes the form:

$$\phi_H = a(y_b) \left[\frac{3 - 2.5\zeta}{1 - 10\zeta + 50\zeta^2} \right]^{\frac{1}{3}} \quad (9)$$

with $a = a_0 + a_1y_b$. It is estimated that $a_0 = 0.48$ and $a_1 = 1.8$. The model is shown in Figure 3c.

4.2 | Stable regime

Given the historically accepted linear nature of the flux-gradient relations in the stable regime (when Ri and Ri_f are below 0.25), also supported by the ensemble data, as well as the role of turbulence anisotropy illustrated in the previous section, we use here a multilinear regression with ζ and y_b as predictors:

$$\phi = a(y_b) + b(y_b)\zeta, \quad (10)$$

where the parameters a and b are linear functions of anisotropy. The parameters are fit to data for ϕ_M (Figure 3b):

$$a = 0.76 + 1.5y_b,$$

$$b = 6.3 - 4.3y_b, \quad (11)$$

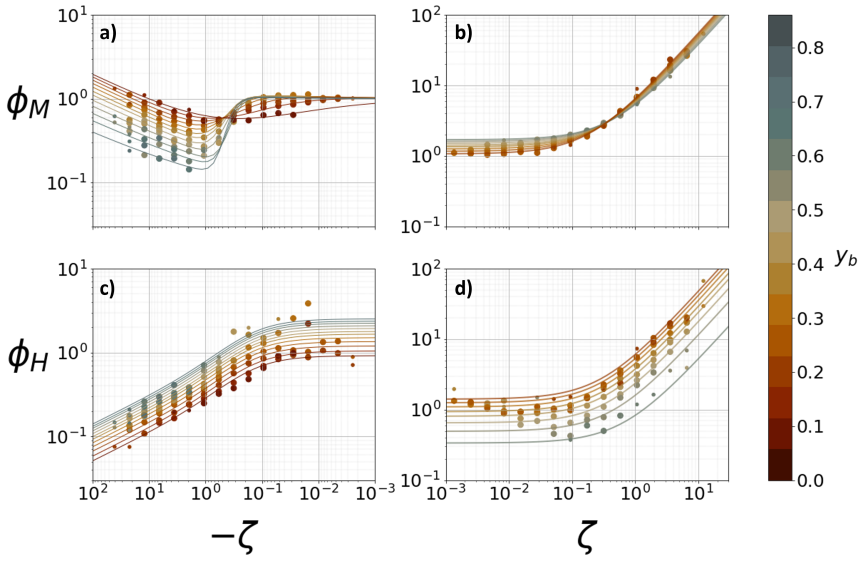


FIGURE 3 The extended flux-gradient universal scaling relations that include the effect of turbulence anisotropy through the degree of anisotropy parameter y_b . Data are binned according to the y_b value (red is anisotropic and dark gray is isotropic turbulence) and ζ , then binned medians are plotted. The corresponding scaling curve for each y_b bin is plotted on top of data. The organization of the panels is the same as in Figures 1 and 2.

and for ϕ_H (Figure 3d):

$$a = \begin{cases} 1.9 - 2.6y_b & y_b < 0.6 \\ 0.34 & y_b > 0.6 \end{cases}, \tag{12}$$

$$b = 6.7 - 10y_b.$$

where a is again constrained to be positive.

4.3 | Implications of the new scaling relations

The new flux-gradient relations for windspeed and temperature highlight a number of interesting features. All the parametrizations show that more anisotropic turbulence is closer to the existing scaling relations, while the quasi-isotropic turbulence shows large deviations. In particular, the parametrization for ϕ_M in the unstable regime supports the existence of three sub-layers (dynamic, dynamic-convective and convective) introduced by KY90, and shows that the scaling curves follow the general scaling prescribed by Kader and Yaglom (1990), however, the ranges of ζ for each sub-layer depend on turbulence anisotropy. Thus, the more anisotropic turbulence is closest to the original KY90 curve, and shows the onset of the dynamic-convective sub-layer at smaller $|\zeta|$ than the more isotropic turbulence. In fact, the scaling relations suggest a regime transition at around $-\zeta \sim 0.4$ so that in dynamic sub-layer ϕ_M is larger for less anisotropic turbulence, whereas in dynamic-convective and convective sub-layers the opposite is the case. Interestingly, the same is true also in the stable regime, where ϕ_M shows a dependence on anisotropy that changes at around $\zeta \sim 0.3$. Thus ϕ_M is proportional to y_b in dynamic regime where buoyancy effects are of lesser importance,

and decreases with increasing y_b in conditions when buoyancy cannot be neglected.

For the temperature gradient the results are different, and there is no clear indication of regime transitions. However, the results show the opposite impact of anisotropy in unstable and stable stratification. In the unstable regime ϕ_H is proportional to y_b and thus a higher ϕ_H is observed for isotropic turbulence, whereas in stable stratification more isotropic turbulence occurs with smaller ϕ_H . In the stable regime the slope of the stability correction is strongly modulated by y_b , with the limit of a zero slope for very isotropic turbulence ($y_b > 0.6$). Finally, it is important to note that the neutral limit of the temperature parameterizations is not continuous between stable and unstable regime, unless only anisotropic turbulence is considered.

5 | DISCUSSION AND IMPLICATIONS FOR EARTH SYSTEM MODELS

5.1 | Model performance and crossvalidation

To assess the improvement in the performance of the newly developed flux-gradient scaling relations for windspeed and temperature (Equations 8,9,10), we calculate the skill score (see Sec. 2.3) in comparison to the classic Businger-Dyer relations, as refitted by HÖ96.

The skill score is assessed separately for each non-dimensional gradient and for the stable and unstable regimes first, and then by separating data into the very unstable ($\zeta < -0.1$), near-neutral unstable ($-0.1 < \zeta < 0$), near-neutral stable ($0 < \zeta < 0.1$) and very stable ($\zeta > 0.1$) regimes (Table 5). The results show a clear improvement brought about by extending flux-gradient scaling relations to include anisotropy. Particularly large improvement is observed in unstable stratification, where the new model consistently outperforms HÖ96 both for wind speed and temperature. In this regime the biggest improvement is seen for temperature under very unstable conditions. In the stable regime the best improvement for wind speed is in the neutral regime, while the opposite happens for temperature. For the stable regime ϕ_H , comparing the model to the HÖ96 parametrizations leads to a major artificial increase in performance, since the slope of HÖ96 is not supported by the data (Figure 2). Still, if the performance reference is taken as the linear model $\phi_H = a + b\zeta$ fitted to the entire ensemble dataset, the resulting skill score is 0.08, still supporting the improvement created by our model against a Businger-Dyer model.

Since each dataset had different number of data points when merged into the ensemble, and so different weights were given to each dataset, we tested every ensemble model (model for wind speed and temperature, for stable and unstable stratification) against the average model obtained for each individual dataset using Student's t-test on every model coefficient, as described in Section 2.3. The test was passed for every parameter for ϕ_M in both regimes and for ϕ_H in stable regime. In the unstable regime, the model for temperature lead to incompatible values, meaning that consistent dataset differences are present that do not average out in the ensemble data. This might indicate that the temperature model in the unstable regime is the least robust, or the most site dependent, of the four, or could be caused by underestimation of the parameters' variance.

Since the new scaling relations were trained and tested on the same data, we further examine the improvement brought about by including anisotropy on each individual dataset by using a posteriori leave-one-out cross-validation (see Sec. 2.3). The cross-validation skill scores (Figure 4) show an overwhelming and consistent improvement using the new scaling relations for all stratification regimes and variables over all the datasets, as already observed for the ensemble data. Interestingly, the relatively complex terrain data at T-Rex Central tower consistently shows the largest improvement in ϕ_M over all other datasets. At the same time, as expected for locations with katabatic flows where ζ needs to be augmented with the information on slope angle (cf., Hang et al., 2021), the T-Rex West tower, shows a marginal degradation of performance under stable stratification.

TABLE 5 Skill score of the new scaling relation for ϕ_M and ϕ_H compared to HÖ96 model (Eq. 7). The skill score is calculated on the whole range of ζ first and then again separating each regime into near neutral and very (un)stable ($|\zeta| < 0.1$)

	Unstable		Stable	
	$\zeta < -0.1$	$\zeta > -0.1$	$\zeta < 0.1$	$\zeta > 0.1$
ϕ_M	0.17		0.08	
	0.15	0.19	0.14	0.06
ϕ_H	0.25		0.58	
	0.27	0.10	0.26	0.63

The performance of the new ϕ_H relations in unstable stratification is particularly striking (40%), as the improvements for individual datasets are significantly larger than the overall improvement of the model (25.5%). Generally, classic MOST ϕ_H relations are consistently found to underestimate the surface sensible heat flux and recently machine learning methods have been employed to reduce the error (McCandless et al., 2022). This result can clearly be connected to not separating the different anisotropy regimes when performing the analysis.

One dataset, however, stands out in terms of reduced performance when anisotropy is taken into account, and that is AHATS, whose cross-validation skill score for ϕ_H in the unstable regime is surprisingly low (Figure 4c). This result suggests that the HÖ96 relations outperform the new scaling relations. The potential causes of this discrepancy compared to the other datasets could stem from the fact that the AHATS tower is significantly lower than other towers (8 m compared to 30-50 m for other towers) and thus also has less isotropic data (Stiperski et al., 2021a) in unstable regime ($y_b = [0.1 - 0.3]$). This inconsistency can further explain the results of the previous compatibility test. Limited improvement or slight deterioration of the results is also found for individual towers under stable stratification, where Stiperski et al. (2019) already showed the importance of processes other than anisotropy.

Apart from these cases, crossvalidation shows an overall consistent improvement over classic formulations, even when these formulations were refit, which reinforces the use of the ensemble trained parametrizations of Section 3 as a compromise between different sites characteristics and flow conditions.

5.2 | Effect of x_b in stable regime

In developing a model for the flux-gradient relations that includes turbulence anisotropy as a scaling parameter, only the degree of anisotropy through the y_b coordinate of the barycentric map (cf. Section 2.1) was considered, leaving out information on the componentiality of the stress tensor (x_b). One could, legitimately, wonder what would be the effect of including the x_b coordinate into the newly developed scaling relations. The effect of x_b , however, can be relevant only in conditions where x_b and y_b are uncorrelated, which is only true for the stable regime. In fact, calculating the Pearson correlation coefficient ρ between x_b and y_b separately for the unstable and stable regime results in $\rho = 0.4$ (unstable) and $\rho = -0.03$ (stable).

To include x_b in the stable regime scaling relations, Equation 10 was modified as:

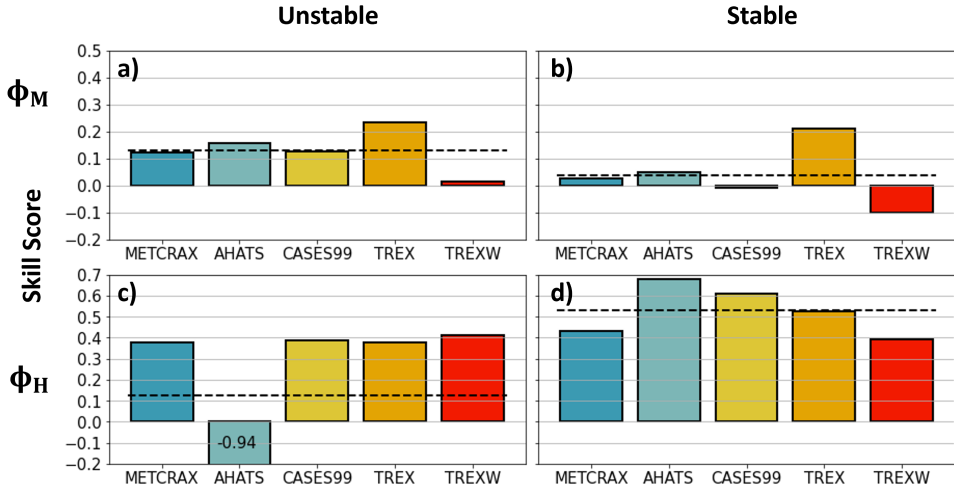


FIGURE 4 Individual skill score of the leave-one-out crossvalidation for ϕ_M (a,b) and ϕ_H (c,d) for unstable (a,c) and stable (b,d) stratification. Skill score is calculated as in Equation 7. The horizontal black line shows the average cross-validation performance.

$$\phi = a(x_b, y_b) + b(x_b, y_b)\zeta, \quad (13)$$

where

$$\begin{aligned} a &= a_0 + a_1 y_b + a_2 x_b, \\ b &= b_0 + b_1 y_b + b_2 x_b, \end{aligned} \quad (14)$$

and fitted to the data for both ϕ_M and ϕ_H .

Fitting the model to the ensemble data shows no improvement in the performance. In fact, the skill-score decreases by 0.002 (0.2%) for the stable windspeed gradient model and increases by 0.005 (0.5%) for the stable temperature gradient model.

This analysis concludes that the effect of x_b in the scaling relations for ϕ_M and ϕ_H is negligible.

5.3 | Scaling components analysis

While the new scaling relations show a clear stratification according to anisotropy, thus hinting at the different ABL structure and dynamics for the different anisotropy types, it still remains unclear if the fluxes or gradients are affected more by anisotropy and in what way. We therefore find it instructive to investigate the dependence of each individual dimensional component that forms each scaling relation on anisotropy. While this approach is clearly limited, since the variables are dimensional and can acquire a range of values, it can still offer insight into the ABL structure. Figure 5 thus shows the dependence of ϕ_M , u_* and $\frac{du}{dz}$ on ζ and y_b , while Figure 6 shows the dependence of ϕ_H , $\overline{w\theta}$ and $\frac{d\theta}{dz}$ on ζ and y_b .

In the convective region of the unstable regime (Figure 5a,c,e), when $\zeta \rightarrow -\infty$, u_* decreases to values around 0.1, while the temperature gradient and the buoyancy flux are asymptotically constant (Figure 6a,c,e), meaning that close to the surface where our data reside the increasing dynamic instability is driven by a decreasing dynamic forcing and not by an increasing buoyancy forcing. The rise of ϕ_M predicted by Kader and Yaglom (1990) for $\zeta < -1$ and observed in our data are shown to stem from the windspeed gradient being almost constant, while the u_* is monotonically decreasing. In this range, isotropic turbulence (high y_b , dark gray) exhibits larger momentum flux and smaller kinematic buoyancy flux, as well as smaller windspeed and temperature gradients than its anisotropic counterpart, which explains the stratification with y_b observed in the convective regime (cf., Figure 2). Still, the drop in the gradients rather than the change in the fluxes in isotropic versus anisotropic turbulence appears to be the driving mechanisms in the observed dependence of scaling relations on anisotropy.

In near-neutral unstable conditions, where $\zeta \rightarrow 0^-$, the buoyancy flux tends to zero faster than the temperature gradient in a well defined way for any degree of anisotropy, while u_* approaches one, thus leading to a neutral limit:

$$\lim_{\zeta \rightarrow 0^-} \phi_H(\zeta) > 1.$$

A similar result was highlighted by Tampieri et al. (2009), Sfyri et al. (2018) and Stiperski and Calaf (2023) for the scaling of the temperature variance. This result implies a turbulent Prandtl number, Pr_t , greater than unity in the near-neutral unstable limit, that is an increasing function of y_b (see Sec. 5.4). In the unstable regime $\frac{d\theta}{dz}$ is constant with ζ when decomposed into anisotropy bins, while its neutral limit decrease is uncertain and not consistent. This uncertainty (also encountered in the stable neutral limit) arises from the unclear nature of the neutral limit in the surface layer and the difficulties of fitting almost constant temperature profiles. In conditions of very small $|\zeta|$ the typical profile of temperature is overall constant with height, but oscillations at the scale of ten meters without a change in the buoyancy flux sign are present, which increase the difficulty in the determination of $\lim_{\zeta \rightarrow 0} \frac{d\theta}{dz}$. This explains the difficulty in determining the unstable neutral limit for ϕ_H and Pr_t .

In the near-neutral range of the stable regime (Figure 5b,d,f), where $0 < \zeta < 0.1$, u_* and $\frac{du}{dz}$ decrease almost in parallel, while in the stable range, where $\zeta > 0.1$, the wind speed gradient increases with increasing stability while u_* decreases faster than in the neutral range. This behavior leads to the linear dependence of ϕ_M on ζ . This result implies that in the very stable boundary layer wind shear is still present but turbulence suppression by buoyancy limits the surface stress u_* . In particular, u_* exhibits a change of behaviour when $\zeta \geq 0.1$ with isotropic turbulence having a larger u_* and tending to zero slower than anisotropic turbulence. In this intermediate stability regime the kinematic buoyancy flux has a peak as showed by Grachev et al. (2005), which happens at lower stability for anisotropic turbulence ($\zeta \sim 0.05$) than for isotropic turbulence ($\zeta \sim 0.5$), as shown by the arrows in Figure 6d. The temperature gradient, however, increases with stability in the stable boundary layer, as expected. Still, isotropic turbulence exhibits lower temperature gradients than the anisotropic one, driving the behaviour of ϕ_H .

5.4 | Eddy diffusivities and the turbulent prandtl number

Eddy diffusivities for momentum, K_m , and heat, K_h , describe the rate at which turbulent eddies transport these two quantities across a fluid medium. They are a product of K-Theory (Stull, 1988), a first order turbulence closure model, formulated as:

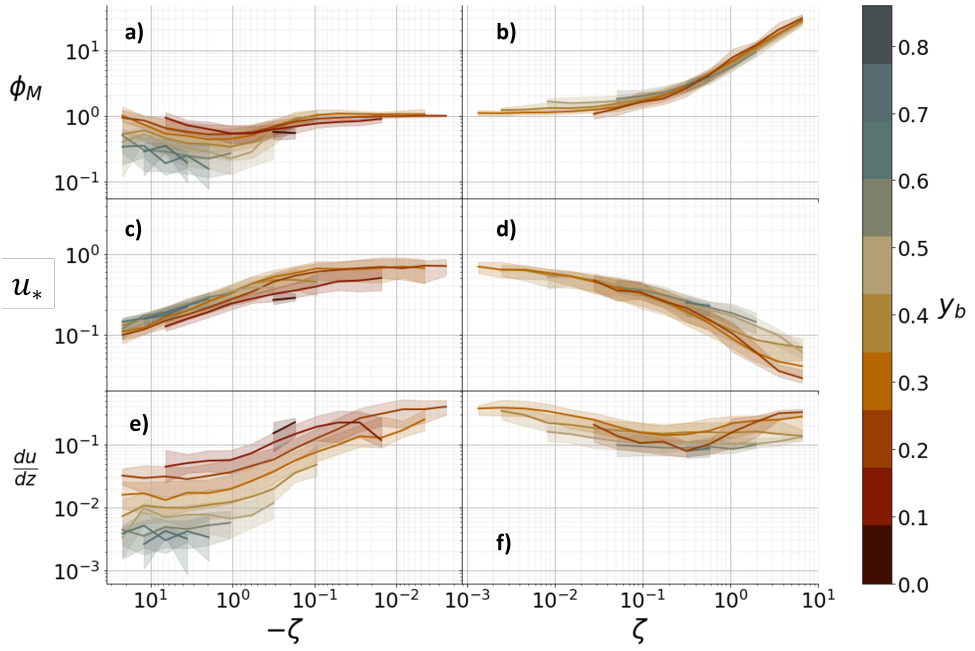


FIGURE 5 The components of the scaling relation for ϕ_M are shown with their dependence on ζ and y_b for both the stable (right column) and unstable (left column) regime.

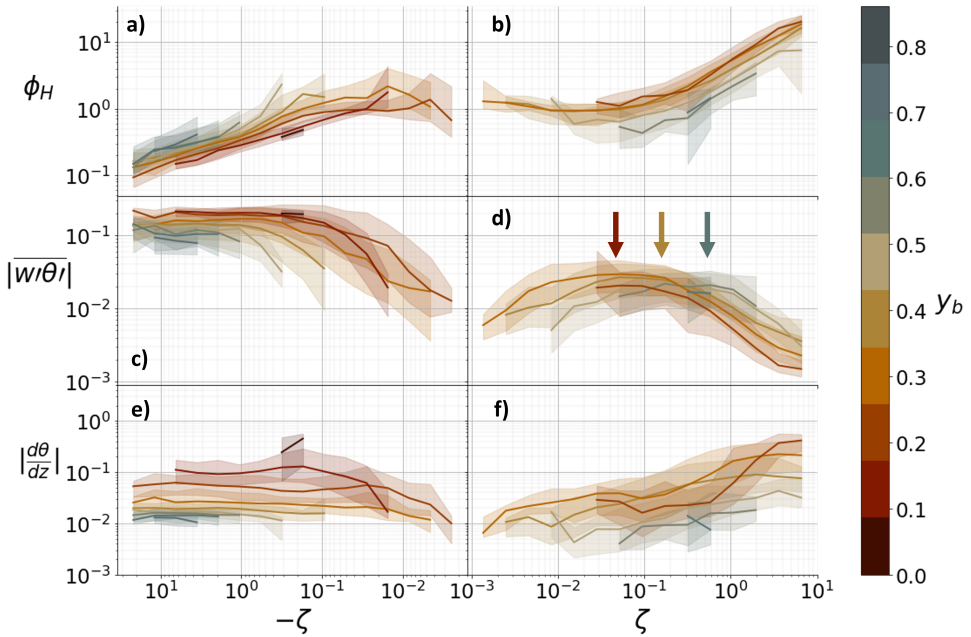


FIGURE 6 The components of the scaling relation for ϕ_H are shown with their dependence on ζ and y_b for both the stable (right column) and unstable (left column) regime.

$$\begin{aligned}\overline{u'w'} &= -K_m \frac{d\bar{u}}{dz}, \\ \overline{w'\theta'} &= -K_h \frac{d\bar{\theta}}{dz},\end{aligned}\tag{15}$$

and are still widely used in observations and boundary layer schemes in numerical models to calculate the turbulent fluxes from the profiles of mean wind speed and temperature. Under the assumption that the mean shear and stress tensor are aligned ($u_s^2 \sim -\overline{u'w'}$ when streamline coordinates are used), the eddy diffusivities can be related to flux-gradient relations (Equation 1) in the following way:

$$\begin{aligned}K_m &= \frac{u_s k z}{\phi_m}, \\ K_h &= \frac{u_s k z}{\phi_h}.\end{aligned}\tag{16}$$

Given the strong dependence of ϕ_M and ϕ_H on anisotropy, it is instructive to explore the dependence of eddy diffusivities on anisotropy as well.

First order closure boundary layer schemes use the TKE (determined either diagnostically, prognostically or iteratively) together with a length scale, to parameterize the eddy diffusivities and calculate the turbulent fluxes from the mean gradients (see Maroneze et al., 2021, for a comparison of state of the art schemes). We therefore investigate the dependence of K_m and K_h on $q = \sqrt{TK\bar{E}}$ and y_b (Fig. 7). The dependence of both K_h and K_m on y_b is stronger under unstable conditions, where anisotropy is as important as TKE, accounting for more than an order of magnitude of variability in K . In the stable regime on the other hand, only K_h shows significant dependence on y_b under conditions of well developed turbulence (higher q). Independently from the stability regime and the magnitude of the effect of anisotropy on eddy diffusivities, it is generally true that both K_m and K_h for isotropic turbulence are higher than for anisotropic turbulence. Figure 7 shows that the dependence of the eddy diffusivities on q is consistent when turbulence anisotropy is taken into account. While in most numerical schemes K_h and K_m are parameterized as functions of q or q^{-1} the available data suggests a power law closer to q^2 , i.e. a linear dependence on TKE, and an increasing function of y_b especially relevant in unstable conditions.

The analysis of the eddy diffusivities highlights an important feature of turbulence in the surface layer: isotropic turbulence is generally more efficient at transporting momentum and heat down-gradient than its anisotropic counterpart for the same stability conditions (ζ , not shown) or turbulent energy ($TK\bar{E}$). In essence, isotropic turbulence can either produce more momentum (buoyancy) flux for the same gradient or produce the same momentum (buoyancy) flux with lower gradients than anisotropic turbulence. Still the results of section 5.3 should be kept in mind, showing that isotropic turbulence generally exists in conditions of lower gradients and fluxes.

We saw in Sections 1 and 3 that the turbulent Prandtl number Pr_t plays a crucial role in explaining the power law of the scaling relation in unstable stratification. We thus explore the dependence of Pr_t on anisotropy. Pr_t represents the ratio of diffusivities of momentum and heat, and is defined as:

$$Pr_t = \frac{K_m}{K_h} = \frac{\phi_h}{\phi_m}.\tag{17}$$

Figure 8 shows the dependence of Pr_t on stability and anisotropy in the ensemble data. The data show substantial scatter, especially in near neutral conditions as reported by Li (2019) and follow the theoretical curve from HÖ96

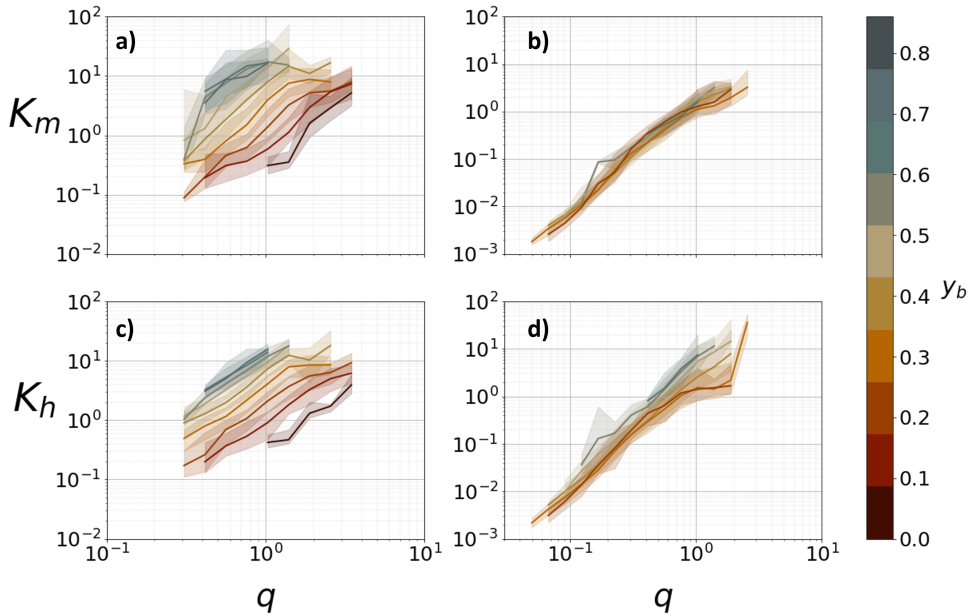


FIGURE 7 Eddy diffusivities for momentum (a,c) and heat (b,d) under unstable (a,c) and stable (b,d) conditions, as defined in Eq. 16. Data are binned according the y_b , while medians of the logarithmically binned ζ are shown in full line, and inter-quartile range in shading.

poorly. Still, as expected, in near-neutral unstable conditions turbulence mixes momentum better than heat, while the opposite happens in the very unstable regime ($\zeta < -1$) and in the stable regime. None the less, the data show that the turbulent Prandtl number has a strong dependence on turbulence anisotropy, which accounts for up to an order of magnitude of variation in the convective regime. The results clearly show that Pr_t approaches zero when $\zeta \rightarrow -\infty$, which contradicts the fundamental assumption of the O'KEYPS equation of a constant asymptotic limit. This is fundamentally linked to the power law of ϕ_M in the convective regime: data clearly shows that ϕ_M is following a $-\zeta^{1/3}$ power law as supported by scaling arguments (cf. Section 3), while ϕ_H follows a well agreed upon $-\zeta^{-1/3}$ power law, leading to a vanishing denominator in Pr_t .

Finally, it is interesting to notice the opposite role of isotropic structures in the stable and unstable boundary layer: in unstable conditions, given the same ζ , Pr_t for isotropic turbulence, i.e. the ratio of the efficiencies of mixing momentum versus heat, is much greater compared to anisotropic turbulence. Alternatively, in the stable regime the opposite happens: isotropic turbulence exhibits a lower Pr_t than anisotropic turbulence.

6 | CONCLUSIONS

This work presents a generalization of flux-gradient relations of the Monin-Obukhov similarity theory outside of its original range of applicability. The new scaling relations for the non-dimensional wind shear ϕ_M and temperature gradient ϕ_H were developed by including the degree of anisotropy as an additional parameter to the local similarity scaling framework, following the work of Stiperski and Calaf (2023). In the unstable regime ($\zeta < 0$) the dependence on anisotropy was added to the model of Kader and Yaglom (1990), while in the stable regime ($\zeta > 0$) a multivariate

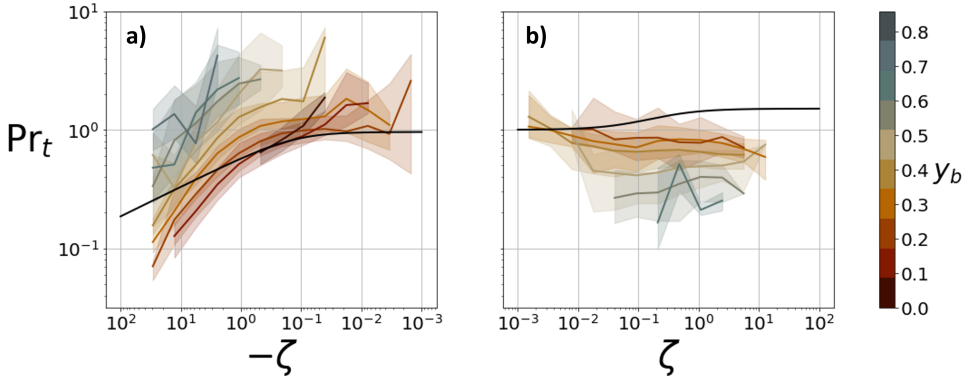


FIGURE 8 The turbulent Prandtl number under unstable (a) and stable (b) conditions, as defined in Eq. 17. Data are binned according to y_b , while medians of the logarithmically binned ζ are shown in full line, and inter-quartile range in shading. The black solid line represents the HO96 model.

linear model was used. The new scaling relations show substantial improvement over classic MOST formulations and were shown to explain majority of the observed scatter in the flux-gradient relations. The improvement was especially large in highly convective conditions, and for scaled temperature gradient ϕ_H in both the unstable and stable regime. This clear dependence of ϕ_H on the degree of anisotropy explains the commonly observed large scatter in ϕ_H and therefore also the large uncertainty of heat fluxes derived from it. Finally, the inclusion of the componentality of turbulence through the first invariant of the barycentric map x_b did not lead to significant improvement in stable stratification, and was therefore not considered further.

The novel scaling additionally allowed to unravel some important features of the atmospheric boundary layer. In particular, they were able to resolve the long standing debate on the correct power law of ϕ_M in the free convective limit ($\zeta < -1$). Our results show that in contrast to analytical models based on the O'KEYPS equation, the correct power law is given by $\phi_M \sim -\zeta^{1/3}$ as predicted by Kader and Yaglom (1990). Additionally, the analysis showed that this rise in ϕ_M in highly convective conditions stems from the flattening of the wind shear for $\zeta \rightarrow -\infty$, while u_* approaches zero. In unstable regime isotropic turbulence was also shown to have a lower wind shear and temperature gradient, and lower heat flux than anisotropic turbulence. The analysis of eddy diffusivities for momentum and heat showed a clear dependence on anisotropy and higher values for more isotropic turbulence, meaning that isotropic turbulence is in general more efficient at creating mixing while existing in conditions of smaller gradients and smaller fluxes. On the other hand, in the stable regime, isotropic turbulence occurred under similar wind speed conditions as anisotropic turbulence, with similar wind shear and slightly higher friction velocity in very stable stratification and consistently lower temperature gradients. The buoyancy flux $\overline{w'\theta'}$ achieved its maximum values (cf., Grachev et al., 2005) at different stability according to turbulence anisotropy: the maximum in $\overline{w'\theta'}$ was at $\zeta \approx 0.05$ in very anisotropic turbulence while for quasi-isotropic turbulence it occurred at $\zeta \approx 0.5$. In this regime the dependence on anisotropy of the eddy diffusivities is much weaker than in the unstable regime, with a strong dependence on TKE. The turbulent Prandtl number was shown to go to zero in the free convective regime, in contrast with the assumption of the O'KEYPS equation, and to have different behaviors in the two regimes: in unstable conditions isotropic turbulence is associated with a higher Prandtl number while the opposite happens in the unstable regime.

The new scaling relations and the conclusions derived from them show robust and promising pathways for the study of boundary layer turbulence. Still, a number of limitations inherent to the MOST approach remain, especially

prominent in stable stratification. The commonly applied quality criteria used in all scaling studies, including the present one, do not allow a thorough study of the full range of conditions encountered in the atmospheric boundary layer. For example, stationary data are only observed in a small fraction of cases in stable stratification. In addition, counter-gradient fluxes, which tend to happen during nighttime and produce positive buoyancy flux with very anisotropic, mostly one-component, turbulence, are excluded from the present analysis as they would be erroneously classified as daytime convective turbulence. There is currently no approach that would allow including them into the MOST framework. Finally, in complex terrain, katabatic winds with a low level jet profile form on slopes during nighttime. The measurements taken above the jet maximum produce a negative wind shear that is filtered out by our quality criteria. Further analysis is therefore needed to explore if a scaling framework for flow above the low level jet maximum could be developed.

In this work we have proposed a generalized flux-gradient formulation of MOST scaling relations, as well as a revised formulation of the first order eddy-diffusivity turbulence closure models based on the inclusion of turbulence anisotropy. This approach has the important advantage of overcoming the traditional canonical limitations of MOST formulation, where the assumptions of horizontal homogeneity are embedded. The new generalized scaling relations represent a leap forward in the way that surface boundary conditions are represented in ESMs at all grid scales, delivering a more accurate representation of the momentum, energy, and mass exchanges at the land-atmosphere interfaces, at the expense of an additional unknown, that is turbulence anisotropy. From a practical standpoint, the question that remains, is how to determine turbulence anisotropy on-the-fly in numerical simulations, and how will this be affected by the traditional anisotropy of the numerical grids employed in ESMs, and their resolution. Turbulence anisotropy is scale-dependent, and thus its contribution to the overall revised flux-gradient relations will be affected by those factors. Nonetheless, these challenges cannot be studied experimentally through traditional single-tower measurements, but instead require large arrays of turbulence measurements, limiting the experimental analysis. At present, to investigate these remaining challenges we envision different approaches consisting in the use of high resolution numerical simulations, machine learning techniques, Lagrangian averaging schemes, and the use of algebraic stress models, while considering the dependence of turbulence anisotropy on terrain, stability, spectral properties, surface thermal and roughness heterogeneity and many more complex terrain features.

Coupling the extended MOST with reliable complex terrain turbulence anisotropy will fulfill a 21st century milestone in the boundary layer community: develop a scaling framework that works in complex terrain.

references

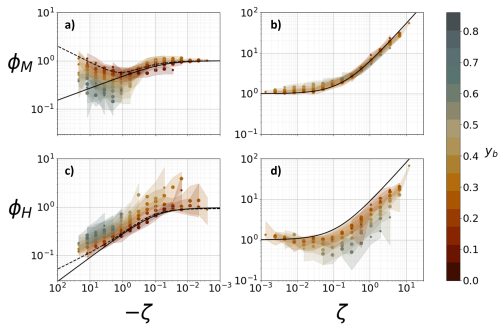
- Babić, K., Rotach, M. W. and Klaić, Z. B. (2016) Evaluation of local similarity theory in the wintertime nocturnal boundary layer over heterogeneous surface. *Agricultural and Forest Meteorology*, **228**, 164–179.
- Babić, N., Večenaj, Ž. and De Wekker, S. F. J. (2016) Flux–variance similarity in complex terrain and its sensitivity to different methods of treating non-stationarity. *Boundary-Layer Meteorology*, **159**, 123–145.
- Banerjee, S., Krahl, R., Durst, F. and Zenger, C. (2007) Presentation of anisotropy properties of turbulence, invariants versus eigenvalue approaches. *Journal of Turbulence*, N32.
- Barskov, K., Glazunov, A., Repina, I., Stepanenko, V., Lykossov, V. and Mammarella, I. (2018) On the applicability of similarity theory for the stable atmospheric boundary layer over complex terrain. *Izvestiya, Atmospheric and Oceanic Physics*, **54**, 462–471.
- Beljaars, A. and Holtslag, A. (1991) Flux parameterization over land surfaces for atmospheric models. *Journal of Applied Meteorology and Climatology*, **30**, 327–341.

- Bou-Zeid, E., Anderson, W., Katul, G. G. and Mahrt, L. (2020) The persistent challenge of surface heterogeneity in boundary-layer meteorology: a review. *Boundary-Layer Meteorology*, **177**, 227–245.
- Boyko, V. and Vercauteren, N. (2023) A stochastic stability equation for unsteady turbulence in the stable boundary layer. *Quarterly Journal of the Royal Meteorological Society*.
- Brutsaert, W. (1992) Stability correction functions for the mean wind speed and temperature in the unstable surface layer. *Geophysical research letters*, **19**, 469–472.
- Businger, J. A., Wyngaard, J. C., Izumi, Y. and Bradley, E. F. (1971) Flux-profile relationships in the atmospheric surface layer. *Journal of the Atmospheric Sciences*, **28**, 181–189.
- Calaf, M., Vercauteren, N., Katul, G. G., Giometto, M. G., Morrison, T. J., Margairaz, F., Boyko, V. and Pardyjak, E. R. (2023) Boundary-layer processes hindering contemporary numerical weather prediction models. *Boundary-Layer Meteorology*, **186**, 43–68.
- Casasanta, G., Sozzi, R., Petenko, I. and Argentini, S. (2021) Flux-profile relationships in the stable boundary layer—a critical discussion. *Atmosphere*, **12**, 1197.
- Cheng, Y. and Brutsaert, W. (2005) Flux-profile relationships for wind speed and temperature in the stable atmospheric boundary layer. *Boundary-Layer Meteorology*, **114**, 519–538.
- Edwards, J. M., Beljaars, A. C. M., Holtslag, A. A. M. and Lock, A. P. (2020) Representation of boundary-layer processes in numerical weather prediction and climate models. *Boundary-Layer Meteorology*, **177**, 511–539.
- Foken, T. (2006) 50 years of the monin-obukhov similarity theory. *Boundary-Layer Meteorology*, **119**, 431–447.
- Foken, T. and Wichura, B. (1996) Tools for quality assessment of surface-based flux measurements. *Agricultural and forest meteorology*, **78**, 83–105.
- de Franceschi, M., Zardi, D., Tagliuzucca, M. and Tampieri, F. (2009) Analysis of second – order moments in surface layer turbulence in an Alpine valley. *Quarterly Journal of the Royal Meteorological Society*, **135**, 1750–1765.
- Grachev, A., Fairall, C. and Bradley, E. (2000) Convective profile constants revisited. *Boundary-layer meteorology*, **94**, 495–515.
- Grachev, A. A., Andreas, E. L., Fairall, C. W., Guest, P. S. and Persson, P. O. G. (2013) The critical richardson number and limits of applicability of local similarity theory in the stable boundary layer. *Boundary-layer meteorology*, **147**, 51–82.
- Grachev, A. A., Fairall, C. W., Persson, P. O. G., Andreas, E. L. and Guest, P. S. (2005) Stable boundary-layer scaling regimes: The SHEBA data. *Boundary-layer meteorology*, **116**, 201–235.
- Grubišić, V., Doyle, J. D., Kuettner, J., Mobbs, S., Smith, R. B., Whiteman, C. D., Dirks, R., Czyzyk, S., Cohn, S. A., Vosper, S. et al. (2008) The terrain-induced rotor experiment: A field campaign overview including observational highlights. *Bulletin of the American Meteorological Society*, **89**, 1513–1534.
- Gryanik, V. M., Lüpkes, C., Grachev, A. and Sidorenko, D. (2020) New modified and extended stability functions for the stable boundary layer based on sheba and parametrizations of bulk transfer coefficients for climate models. *Journal of the Atmospheric Sciences*, **77**, 2687–2716.
- Hang, C., Oldroyd, H. J., Giometto, M. G., Pardyjak, E. R. and Parlange, M. B. (2021) A local similarity function for katabatic flows derived from field observations over steep-and shallow-angled slopes. *Geophysical Research Letters*, **48**, e2021GL095479.
- Hastie, T. J. (2017) Generalized additive models. In *Statistical models in S*, 249–307. Routledge.
- Högström, U. (1988) Non-dimensional wind and temperature profiles in the atmospheric surface layer: A re-evaluation. In *Topics in Micrometeorology. A Festschrift for Arch Dyer*, 55–78. Springer.

- (1996) Review of some basic characteristics of the atmospheric surface layer. *Boundary-Layer Meteorology*, **78**, 215–246.
- Howell, J. and Mahrt, L. (1997) Multiresolution flux decomposition. *Boundary-Layer Meteorology*, **83**, 117–137.
- Huber, P. J. (1992) Robust estimation of a location parameter. In *Breakthroughs in statistics: Methodology and distribution*, 492–518. Springer.
- Kader, B. and Perepelkin, V. (1989) Effect of unstable stratification on the wind speed and temperature profiles in the surface layer. *Atmos. Oceanic Phys*, **25**, 583–588.
- Kader, B. and Yaglom, A. (1990) Mean fields and fluctuation moments in unstably stratified turbulent boundary layers. *Journal of Fluid Mechanics*, **212**, 637–662.
- Katul, G. G., Konings, A. G. and Porporato, A. (2011) Mean velocity profile in a sheared and thermally stratified atmospheric boundary layer. *Physical review letters*, **107**, 268502.
- Klipp, C. L. and Mahrt, L. (2004) Flux–gradient relationship, self-correlation and intermittency in the stable boundary layer. *Quarterly Journal of the Royal Meteorological Society: A journal of the atmospheric sciences, applied meteorology and physical oceanography*, **130**, 2087–2103.
- Kolmogorov, A. N. (1941) The local structure of turbulence in incompressible viscous fluid for very large reynolds numbers. *Cr Acad. Sci. URSS*, **30**, 301–305.
- Kral, S. T., Sjöblom, A. and Nygård, T. (2014) Observations of summer turbulent surface fluxes in a High Arctic fjord. *Quarterly Journal of the Royal Meteorological Society*, **140**, 666–675.
- Lehner, M., Whiteman, C. D., Hoch, S. W., Crosman, E. T., Jeglum, M. E., Cherukuru, N. W., Calhoun, R., Adler, B., Kalthoff, N., Rotunno, R. et al. (2016) The METCRAX II field experiment: A study of downslope windstorm-type flows in Arizona's Meteor Crater. *Bulletin of the American Meteorological Society*, **97**, 217–235.
- Li, D. (2019) Turbulent prandtl number in the atmospheric boundary layer—where are we now? *Atmospheric Research*, **216**, 86–105.
- (2021) The o'keeps equation and 60 years beyond. *Boundary-Layer Meteorology*, **179**, 19–42.
- Li, D., Katul, G. G. and Bou-Zeid, E. (2012) Mean velocity and temperature profiles in a sheared diabatic turbulent boundary layer. *Physics of Fluids*, **24**, 105105.
- Lumley, J. L. and Newman, G. R. (1977) The return to isotropy of homogeneous turbulence. *Journal of Fluid Mechanics*, **82**, 161–178.
- Maroneze, R., Acevedo, O. C., Costa, F. D., Puhales, F. S., Anabor, V., Lemes, D. N. and Mortarini, L. (2021) How is the two-regime stable boundary layer reproduced by the different turbulence parametrizations in the weather research and forecasting model? *Boundary-Layer Meteorology*, **178**, 383–413.
- Martí, B., Martínez-Villagrasa, D. and Cuxart, J. (2022) Flux–gradient relationships below 2 m over a flat site in complex terrain. *Boundary-Layer Meteorology*, **184**, 505–530.
- McCandless, T., Gagne, D. J., Kosovic, B., Haupt, S. E., Yang, B., Becker, C. and Schreck, J. (2022) Machine learning for improving surface-layer-flux estimates. *Boundary-Layer Meteorology*, **185**, 199–228.
- Monin, A. S. and Obukhov, A. M. (1954) Basic laws of turbulent mixing in the surface layer of the atmosphere. *Contrib. Geophys. Inst. Acad. Sci. USSR*, **151**, e187.
- Nadeau, D. F., Pardyjak, E. R., Higgins, C. W. and Parlange, M. B. (2013) Similarity scaling over a steep alpine slope. *Boundary-layer meteorology*, **147**, 401–419.

- Nieuwstadt, F. T. (1984) The turbulent structure of the stable, nocturnal boundary layer. *Journal of Atmospheric Sciences*, **41**, 2202–2216.
- Obukhov, A. (1971) Turbulence in an atmosphere with a non-uniform temperature. *Boundary-layer meteorology*, **2**, 7–29.
- Pope, S. B. (2000) *Turbulent flows*. Cambridge university press.
- Poulos, G. S., Blumen, W., Fritts, D. C., Lundquist, J. K., Sun, J., Burns, S. P., Nappo, C., Banta, R., Newsom, R., Cuxart, J. et al. (2002) CASES-99: A comprehensive investigation of the stable nocturnal boundary layer. *Bulletin of the American Meteorological Society*, **83**, 555–582.
- Salesky, S. T. and Chamecki, M. (2012) Random errors in turbulence measurements in the atmospheric surface layer: implications for monin–obukhov similarity theory. *Journal of the Atmospheric Sciences*, **69**, 3700–3714.
- Salesky, S. T., Katul, G. G. and Chamecki, M. (2013) Buoyancy effects on the integral lengthscales and mean velocity profile in atmospheric surface layer flows. *Physics of Fluids*, **25**, 105101.
- Sfyri, E., Rotach, M. W., Stiperski, I., Bosveld, F. C., Lehner, M. and Obleitner, F. (2018) Scalar-flux similarity in the layer near the surface over mountainous terrain. *Boundary-layer meteorology*, **169**, 11–46.
- Stiperski, I. and Calaf, M. (2018) Dependence of near-surface similarity scaling on the anisotropy of atmospheric turbulence. *Quarterly Journal of the Royal Meteorological Society*, **144**, 641–657.
- (2023) Generalizing monin-obukhov similarity theory (1954) for complex atmospheric turbulence. *Physical Review Letters*, **130**, 124001.
- Stiperski, I., Calaf, M. and Rotach, M. W. (2019) Scaling, anisotropy, and complexity in near-surface atmospheric turbulence. *Journal of Geophysical Research: Atmospheres*, **124**, 1428–1448.
- Stiperski, I., Chamecki, M. and Calaf, M. (2021a) Anisotropy of unstably stratified near-surface turbulence. *Boundary-Layer Meteorology*, **180**, 363–384.
- Stiperski, I., Holtslag, A. A. M., Lehner, M., Hoch, S. W. and Whiteman, C. D. (2020) On the turbulence structure of deep katabatic flows on a gentle mesoscale slope. *Quarterly Journal of the Royal Meteorological Society*, **146**, 1206–1231.
- Stiperski, I., Katul, G. G. and Calaf, M. (2021b) Universal return to isotropy of inhomogeneous atmospheric boundary layer turbulence. *Physical Review Letters*, **126**, 194501.
- Stoll, R., Gibbs, J. A., Salesky, S. T., Anderson, W. and Calaf, M. (2020) Large-eddy simulation of the atmospheric boundary layer. *Boundary-Layer Meteorology*, **177**, 541–581.
- Stull, R. B. (1988) *An introduction to boundary layer meteorology*, vol. 13. Springer Science & Business Media.
- Tampieri, F., Maurizi, A. and Viola, A. (2009) An investigation on temperature variance scaling in the atmospheric surface layer. *Boundary-layer meteorology*, **132**, 31–42.
- Wyngaard, J. C. (2010) *Turbulence in the Atmosphere*. Cambridge University Press.
- Zilitinkevich, S., Elperin, T., Kleeorin, N., Rogachevskii, I. and Esau, I. (2013) A hierarchy of energy-and flux-budget (efb) turbulence closure models for stably-stratified geophysical flows. *Boundary-layer meteorology*, **146**, 341–373.

GRAPHICAL ABSTRACT



Monin Obukhov similarity theory (MOST) is widely used in earth system models to parametrize turbulent exchanges in the atmospheric surface layer, however its original range of applicability is limited to flat and homogeneous terrain and a restrictive stability range. In this work we extend the original MOST to complex terrain by including information on turbulence anisotropy into the flux-gradient scaling relations, showing substantial improvement, especially in conditions of unstable stratification.